Academic Journal of Science and Technology
ISSN: 2771-3032 | Vol. 14, No. 1, 2025

Study on Damage Characteristics of Anchor Cable Anchorage Body Under Different Vibration Loads

Guang Zhao[1, *], Wen Wang[1], Zhenhua Li[1]

[1]School of Energy Science Engineering Henan Polytechnic University, Jiaozuo 454003, China

[*] Corresponding author: Guang Zhao (Email: 13298129775@163.com)

Abstract: In order to explore the damage evolution law of anchorage body under cyclic loading, based on numerical simulation, the mechanical behavior and damage evolution mechanism of anchorage body under different vibration loads are systematically analyzed. The evolution law of fracture field, displacement field, velocity field and force chain is studied. The results show that the crack field evolution of anchorage body can be divided into four stages: crack initiation, crack propagation, crack stable increase and crack coalescence. As the vibration load increases, the number of cracks increases significantly. The increase of the vibration load significantly accelerates the debonding rate of the anchor cable and promotes the damage process of the anchorage body. In addition, the evolution laws of fracture field, displacement field, velocity field and force chain show that the increase of vibration load accelerates the penetration of cracks, which aggravates the failure process of anchorage system. The shear stress is transmitted from shallow to deep, and the shear stress of the first interface is higher than that of the second interface. With the increase of the vibration load, the fracture range of the force chain in the anchorage body gradually expands. Specifically, under the action of 70%F vibration load and 1Hz frequency, the number of cracks is the largest and the degree of damage is the most serious. Under the action of 30%F vibration load and 30Hz frequency, the cracks are mainly concentrated in the anchoring agent ring, and the damage degree of the matrix is lighter. The research results reveal the difference law of crack propagation of anchor cable anchorage structure under different vibration load conditions, which provides a theoretical basis for the optimal design of anchorage system.

Keywords: Cyclic loading; vibration load; fissure evolution; force chain; orthogonal parameters.

1. Introduction

With the gradual exploitation of deep coal resources, dynamic disturbances such as rock burst and mine earthquake have intensified, which seriously threatens the safe production of mines[1].

The anchor cable anchorage structure can play a good supporting effect under static load conditions, while under dynamic load disturbance, the anchorage body is prone to fatigue damage, resulting in the instability of the roadway structure. It is of great significance to explore the internal damage evolution law and failure mode of anchor cable anchorage body under different frequency and energy disturbance conditions for reasonably constructing roadway support system and guiding the development of surrounding rock control technology in deep roadway. In order to understand the dynamic response characteristics and failure mechanism of anchored solid under dynamic load, many scholars have carried out a series of studies through laboratory tests. Ning Jianguo et al.[2] revealed the deformation characteristics of anchor rod in anchored solid under dynamic load and the coordinated deformation relationship between anchor rod and matrix by carrying out impact test of SHPB anchored specimen. Chang et al. [3,4] used SHPB to study the stress wave propagation law and spallation characteristics of anchorage body under different dynamic loads, and clarified the deterioration mechanism of anchorage body. Based on PFC numerical simulation, Zhang Nong et al.[5] revealed the progressive failure mechanism and the attenuation law of bearing capacity of anchorage structure under high-frequency and low-energy impact disturbance for anchorage under different working conditions under impact load. Wu Yongzheng et al. [6] carried out the lateral dynamic load impact test of anchored rock mass, and obtained the dynamic load energy level and the response relationship between the mechanical parameters of the anchor and the dynamic mechanical properties of the anchored rock mass. Wu Qiuhong et al.[7] carried out the dynamic mechanical response characteristics of the full-length bonded anchor with the help of SHPB, and analyzed the failure characteristics of the anchorage body. Chen et al. [8] used the Hopkinson pressure bar test to carry out the dynamic impact test of the anchor body with holes, and studied the influence of the bolt and the prefabricated borehole on the dynamic mechanical properties and fracture law of the sample. In terms of numerical simulation, Li Qinghai et al. [9] studied the non-linear model by numerical simulation. Wang Wenjie et al.[10]used FLAC3D software to establish a numerical calculation model of full-length mortar anchored FRP bolt, and studied the stress and failure characteristics of bolt body, rod body and mortar interface, mortar and surrounding rock interface under static load of pre-tightening force and blasting dynamic load. Wang Aiwen et al. [11] studied the dynamic coupling effect and failure mechanism of bolt-surrounding rock under impact load by numerical simulation, and pointed out that there was an obvious ' time difference effect ' between bolt and surrounding rock vibration under impact load, with the increase of impact velocity. Zhan Yubao et al.[12] through numerical simulation, it is concluded that the distribution of shear stress in anchorage body is very uneven. With the increase of load, the distribution range of shear stress slowly expands downward. The magnitude and distribution of shear stress on anchorage body are closely related to the properties of rock mass. Xue et al.[13] used FLAC numerical simulation software to analyze the influence of seismic load on end anchor and full anchor bolt. It is considered that the

installation angle of anchor bolt is the key influencing factor of axial stress change. The maximum stress in anchor bolt caused by seismic load is lower than the yield strength of anchor bolt. Compared with full anchor bolt, end anchor bolt has higher ductility and is more suitable for resisting dynamic load impact. Zhu Wancheng et al.[14] studied how the dynamic disturbance triggers the occurrence of deep roadway by numerical simulation method.

There have been many studies on the damage and failure of bolt anchorage structure under impact dynamic load, but there are few studies on the internal damage evolution law and failure mode of anchor cable anchorage structure under different frequency and energy impact. Therefore, based on the indoor test of cyclic load disturbance and the numerical simulation of PFC2d, the numerical simulation analysis of static load and cyclic disturbance of anchor cable anchorage body is designed. The damage characteristics of anchorage body and the damage failure mode of anchorage body under different loading modes are analyzed, and the derivation and development law of internal cracks in anchorage body is revealed, which provides a key basis for further exploring the anchorage mechanism of anchor cable.

2. Study on Synergistic Deformation Characteristics of Anchorage Body Under Cyclic Loading

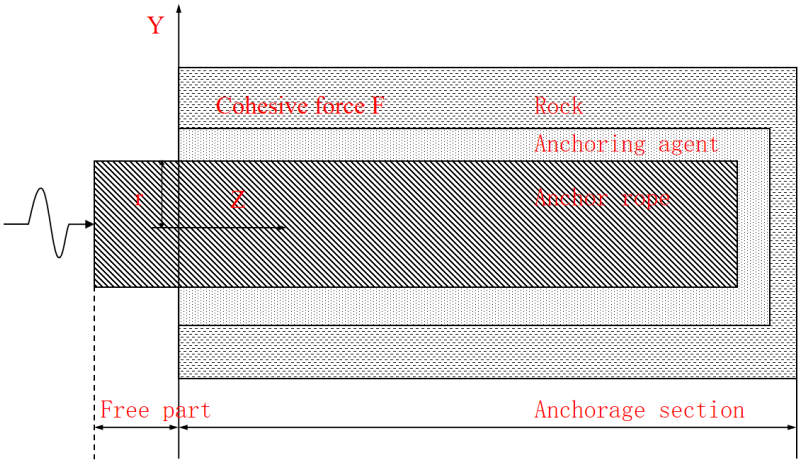

Figure 1. Stress model of anchor cable under cyclic loading

Under the action of dynamic load, the mechanical model of bolt is established, as shown in Fig.1, and the following assumptions are put forward: Both surrounding rock and bolt are regarded as linear elastic materials; The contact surface between surrounding rock and bolt follows Mohr-Coulomb failure criterion; The axial stress distribution on the bolt interface is uniform. It is assumed that the peak velocity of the surrounding rock measuring point is v_{max}. After the dynamic load, the stress change of the point is:

$$\sigma_d(x) = \rho_r c_r v_{\max} \tag{1}$$

In the formula, pris rock density, kg/m3, cris the propagation velocity of longitudinal wave in rock, m /s.

The stress analysis of the anchoring unit is shown in Fig.2, assuming that the relative deformation between the anchoring agent and the rod body is ignored. In the diagram, σ_z (x) represents the cohesive force on the contact surface between the bolt and the surrounding rock, and the unit is MPa. According to the equilibrium equation, the deformation ds_r (x) of surrounding rock under dynamic stress is :

$$ds_r(\mathrm{x}) = \frac{\sigma_z(x) r(1+\mu_r)}{E_r z} dx \tag{2}$$

Where μ_z is the Poisson's ratio of rock;Er is the elastic modulus of rock, MPa.

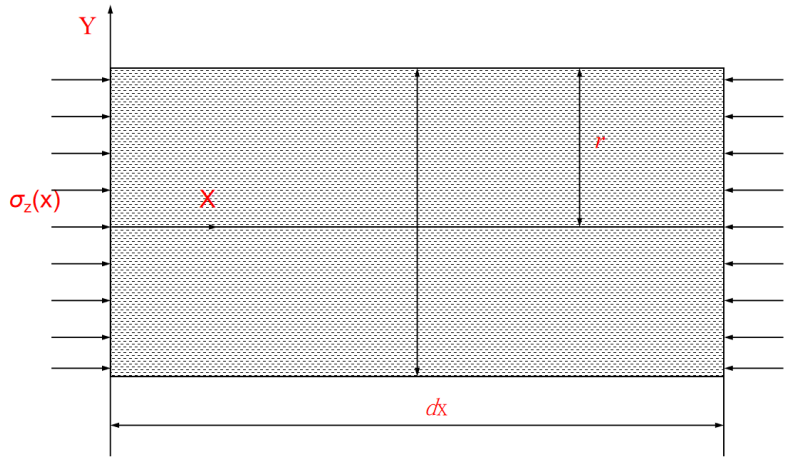

Figure 2. Horizontal force analysis of anchorage micro-unit under cyclic loading

Under the action of dynamic load, the displacement of anchor cable along the axial direction is:

$$ds_b(x) = \frac{1}{E_z}\sigma(x)dx \tag{3}$$

In the formula, E_z is the elastic modulus of anchor cable, MPa ; σ (x) is the axial stress of the anchor cable, MPa.

The stress transfer relationship between the anchor cable and the surrounding rock is affected by the elastic modulus and bonding characteristics of the two. When the cohesive force is strong, the anchor cable can effectively slow down the stress concentration of surrounding rock caused by dynamic load. Under the action of dynamic load, the synergistic effect between anchor cable and surrounding rock plays a key role in structural stability. In this process, the plastic strain of the bonding unit gradually accumulates, and the anchoring agent exhibits obvious plastic damage deformation, resulting in a gradual decrease in the bonding strength. With the continuous development of damage, the anchor cable gradually debonded and slipped, and the displacement increment of the free section of the anchor cable increased significantly, which further aggravated the overall damage of the anchor body. This mechanism reveals the complex interaction of stress, displacement and damage in the anchorage system under dynamic loading conditions.

3. Numerical Modeling

3.1. Modelling

The basic unit in the PFC model is a spherical particle (ball), and different particles are combined by bonding to form a contact (contact). In the simulation of compression test, the boundary wall is defined and the velocity boundary condition is applied to realize the loading. In the process of applying pressure, the force-displacement relationship is used to calculate the contact force of the contact point, and the Newton 's law of motion is used to solve the displacement of the spherical particles. When the load exceeds the bearing limit of the contact bond, the contact will break and form micro cracks, which can analyze the deformation and failure of the structure from the micro level.

3.2. Parameter calibration

At present, researchers generally use the 'trial calculation' method to obtain the microscopic parameters that have a great influence on the macroscopic mechanical parameters, and focus on the calibration of these parameters, so as to quickly match the indoor test results. In this paper, uniaxial compression and direct tensile tests are used to calibrate the parallel bond model. In the uniaxial compression simulation test, the particle discrete element numerical simulation simulates the soft rock medium through the composition of discrete particles, and the accurate calibration of the mesoscopic parameters is crucial to the accuracy of the simulation results. For this reason, a uniaxial compression test model of the anchoring matrix was constructed. The model size was 100mm×100mm, the particle radius was between 1.5mm and 2.0mm, and the porosity was 0.1. After the initial balance is achieved, the left and right walls are removed, the upper and lower walls are retained as the loading wall, and a fixed speed of 0.2m/s is applied to the upper and lower walls for loading. The numerical model of uniaxial test is shown in Fig 3 The comparison of the specimens before and after the failure of the numerical simulation is shown in Fig 4(b). The numerical simulation results are compared with the stress-strain curves of the actual test, and the results are shown in Fig 4 (c).

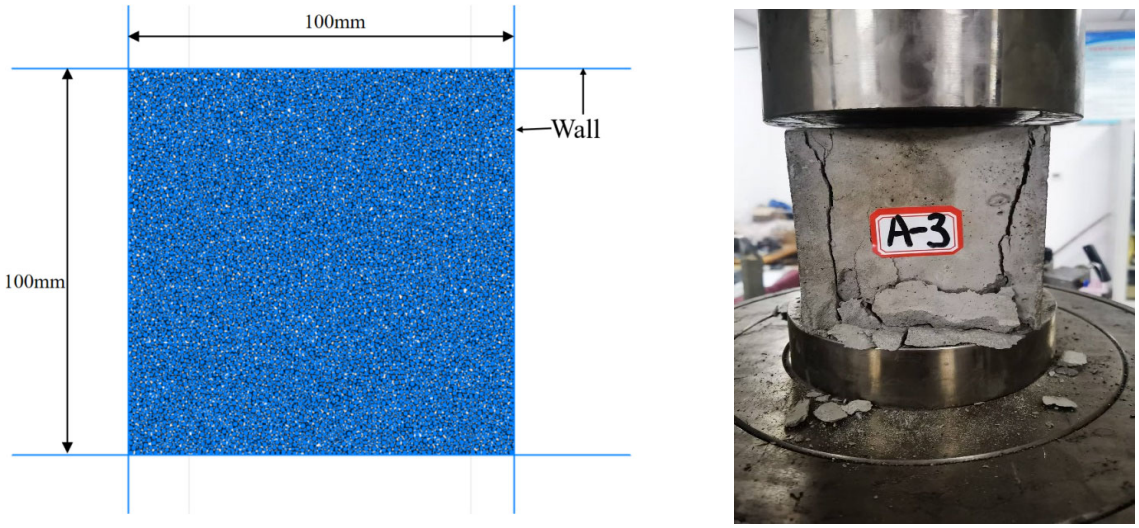

(a) Create a uniaxial specimen model (b) Uniaxial compression test in laboratory

Figure 3. Creation of numerical model of uniaxial test

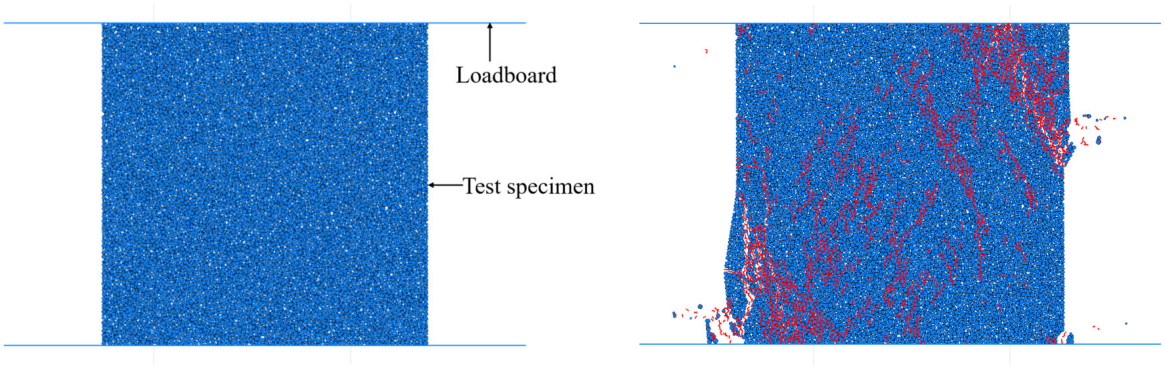

(a) Before loading (b) After loading

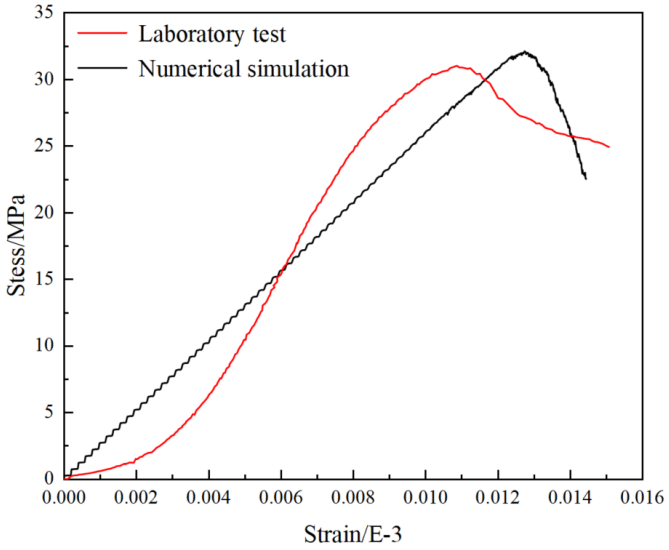

(c) Laboratory test and numerical simulation comparison

Figure 4. Uniaxial compressive strength test

Table 1. Mesoscopic parameters of anchor cable anchorage body

Mesoscopic parameters	Anchoring matrix	anchoring agent	anchor rope
Particle density (kg / m3)	1800	2500	7850
Effective modulus / GPa	6	20	210
Linear contact stiffness ratio	2	2	2
Parallel bond modulus	1	1	200
Tensile strength / MPa	2	8	1860
Compressive strength / MPa	30	6	-
Bond strength / MPa	16.5	10	1860
coefficient of friction	0.5	0.5	0.5

The anchor cable adopts full-length anchoring, the anchoring length is 0.15m, the particle diameter of the model is between 0.0004m and 0.0008m, the porosity is 0.1, and the anchoring surrounding rock and anchoring agent are randomly generated particles (distribute command). The first anchoring interface (anchor cable-anchoring agent interface) and the second anchoring interface (anchoring agent-anchoring matrix interface) are arranged six monitoring circles along the Y axis, with an interval of 30 mm, mainly monitoring the shear stress changes of the first and second interfaces during the loading process. The numerical model of anchored solid is shown in Fig 5. The meso-scale calibration of anchor cable, anchoring agent and surrounding rock in the model is carried out by rapid calibration method. The calibrated meso-scale parameters are shown in Table 1. The cyclic load along the axial direction is applied to the top of the anchor cable. The vibration load applied by the cyclic load is 40%*F*, 50%*F*, and 60%*F*, where F is the ultimate pull-out strength measured by the indoor test of the anchor cable anchor body. In order to ensure that the numerical simulation is consistent with the experimental results, *F* takes the average ultimate pull-out strength of the indoor test of 48KN. The loading frequency is 10Hz, and the loading waveform is a sine wave. The waveform formula is shown in Equation (4).

$$F(x) = A \cdot \sin(2\pi f \cdot x) + B \tag{4}$$

Where A is the amplitude of the applied sine wave, /KN; f is the loading frequency, /Hz; B is the vibration load, /KN.

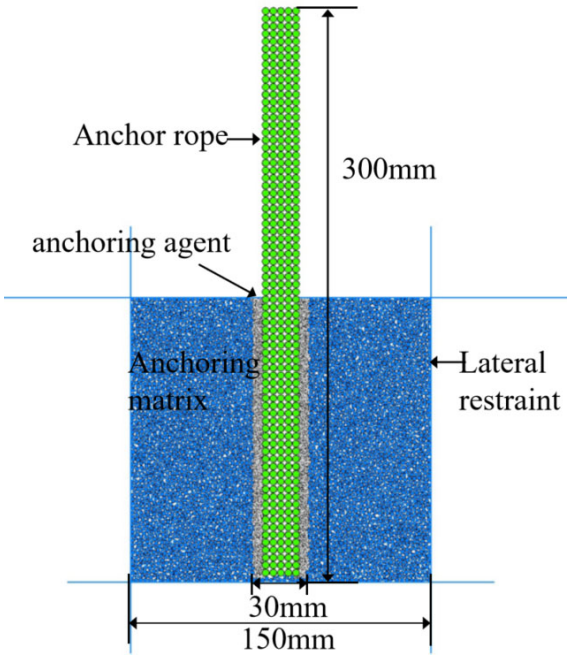

Figure 5. Numerical model of anchorage body under cyclic loading

4. The Influence of Anchor Damage Characteristics Under Different Cyclic Pull-out Loads

4.1. Analysis of progressive failure process of anchorage body

4.1.1. Evolution law of displacement field

In the indoor experiment, the anchorage specimen is placed in a fixed tooling, which is equivalent to imposing constraints on the top and side of the specimen. In order to ensure that the numerical simulation is consistent with the experimental loading process, the numerical model imposes a constraint wall on the side, the bottom surface and the upper end surface of the top of the anchoring agent. The effect of the upper restraint wall makes the maximum change of the vertical displacement appear near the anchorage layer. Under the static load pull-out load, because the bond strength of the first interface of the anchorage is higher than that of the second interface, the anchor cable and the anchorage agent are pulled out together, resulting in the displacement concentrated in the anchorage agent and the surrounding matrix area. Due to the top constraint, the surrounding rock displacement near the orifice is small. During the drawing process, penetrating cracks appeared in the anchorage matrix, and the displacement field gradually evolved from the initial symmetrical distribution to the asymmetric distribution.

As shown in Fig 6, the axial displacement nephograms of 10KN, 20KN, 30KN and 40KN drawing loads are shown respectively. When the drawing load is 10KN, the displacement field of the anchorage body is 'left and right symmetry, the displacement of the middle anchor cable and the anchoring agent side is larger, the displacement on both sides of the matrix gradually decreases, the displacement of the shallow part is larger, and the deep displacement gradually decreases'. This phenomenon indicates that the anchorage body is mainly in the elastic deformation stage at this time, no debonding or bond slip occurs, and the shear deformation between the anchoring agent and the matrix is small. As the drawing load increases to 20KN, the vertical displacement field shows the characteristics of' asymmetry, and the displacement of the anchoring agent and the surrounding matrix is not coordinated', indicating that the system has entered the elastic-plastic deformation stage. At this time, the shallow anchoring interface has been debonding, and the anchoring agent and the nearby matrix have shear deformation and failure. When the load is increased to 30KN, the cloud change of the vertical displacement field almost disappears, and the displacement of the whole anchoring agent is significantly larger than that of the surrounding rock and soil, indicating that the anchoring system has entered the plastic deformation stage. Most of the interface between the anchoring agent and the anchoring matrix is debonding, and there is a significant shear failure between the anchoring agent and the anchoring matrix. Finally, when the drawing load reaches 40KN, the vertical displacement field cloud diagram completely disappears, and there is an obvious uplift phenomenon at the interface between the shallow anchoring agent and the anchoring matrix. The anchoring agent pulls out of the matrix and the bottom is obviously empty. This indicates that the anchorage body is in the debonding failure stage at this time, the interface between the whole anchoring agent and the anchoring matrix has been completely debonded, and the anchoring agent holding anchor cable is completely pulled out.

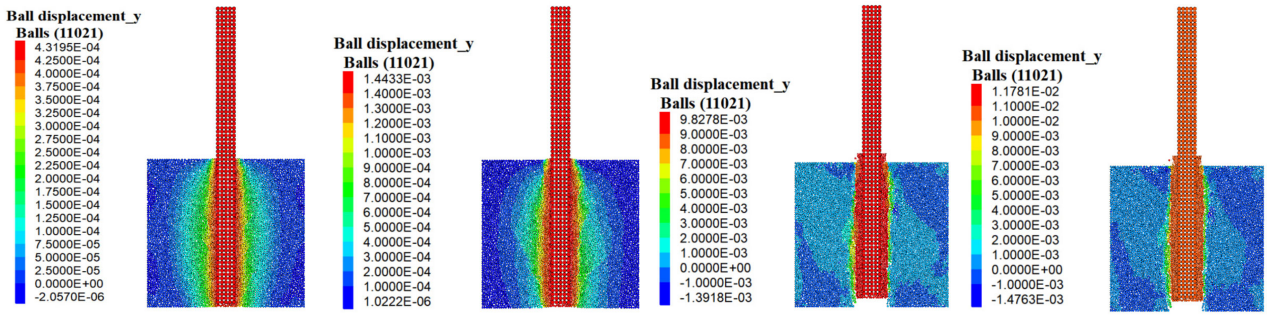

(a) 10KN (b) 20KN (c) 30KN (d) 40KN

Figure 6. Evolution cloud diagram of displacement field of anchorage body under different drawing loads3.1.2 Evolution law of fracture field

As shown in Fig 7, the evolution cloud diagram of the crack field inside the anchorage body at the time of drawing load is shown respectively. The total number of cracks, the evolution law of tensile cracks and shear cracks during the loading process are shown in Fig.8.

From Fig 7, it can be seen that under the action of static load drawing, the cracks first appear at the orifice, and the number of cracks increases with the increase of the loading specimen. When the drawing load is 10KN, the interface between the anchoring agent and the surrounding rock begins to appear cracks and extend to the bottom. When the drawing load is 20KN, the cracks gradually develop along the anchoring depth, the cracks of the surrounding rock at the bottom run through, the anchor cable appears bond slip, the surrounding rock near the anchoring agent appears crack concentration, and the number of cracks continues to increase. When the drawing load is 30KN, the cracks at the end of the anchorage increase greatly, and some surrounding rock carried by the bottom anchoring agent is pulled out together with the anchor cable; when the pull-out load is 40KN, the combination of anchor cable and anchoring agent is pulled out, the bond-slip distance increases gradually, the cracks of surrounding rock increase gradually, and the bottom and top cracks run through the surface of anchored surrounding rock, which is manifested as splitting failure of surrounding rock. The law of fracture development is that the fracture develops from the orifice along the anchorage depth to the end of the anchorage, and develops from the position near the anchor cable to the edge of the surrounding rock in the transverse direction. The cracks mainly appear on the anchorage interface between the anchoring agent and the surrounding rock, and are distributed on both sides of the hole wall.

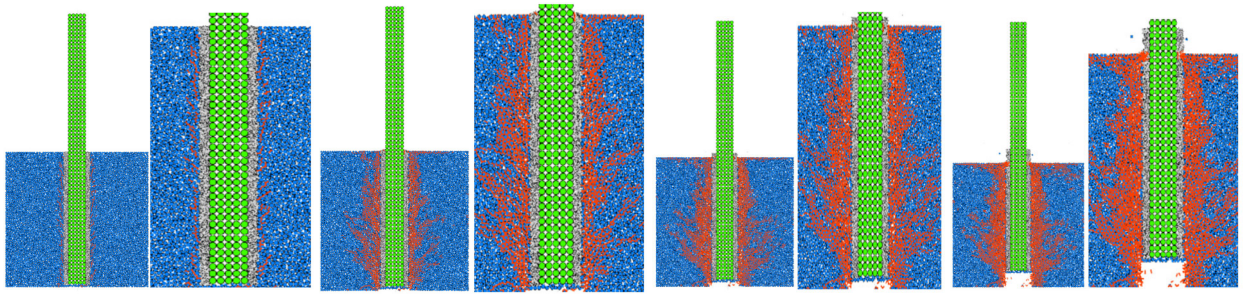

(a) 10KN (b) 20KN (c) 30KN (d) 40KN

Figure 7. Evolution cloud diagram of fracture field

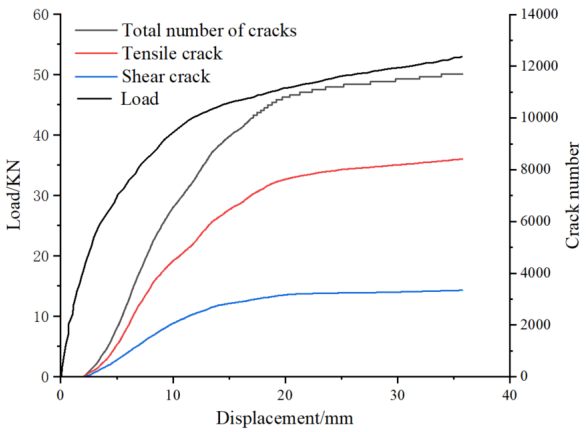

Figure 8. Crack evolution law

It can be seen from Fig 8 that the tensile cracks, shear cracks and the total number of cracks increase rapidly with

the increase of time step, and then the growth rate slows down. The variation curve of the total number of cracks has a good similarity with the change trend of the pull-out load. The' mutation point'of the tensile fracture curve appears at the displacement of the tensile end of about 20mm, while the 'mutation point' of the shear fracture curve appears at the displacement of the tensile end of about 15mm. Therefore, when the displacement of the tensile end is about 15mm and 20mm, there are also two obvious' mutation points' in the curve of the total number of cracks. When the displacement of the tensile end is less than 5mm, there is a linear relationship between the drawing load and the displacement of the tensile end. When the displacement of the tensile end exceeds 5mm but is less than 20mm, the relationship between the two begins to become nonlinear. When the displacement of the tensile end exceeds 20mm, although the displacement of the tensile end increases rapidly, the pull-out load increases almost linearly and the growth rate is very slow, indicating that the anchorage system has shown signs of damage at this time. When the displacement of the tensile end exceeds 20mm, the change rate of the number of tensile cracks and shear cracks is close, and the growth trend of the two is consistent.

4.2. The evolution law of fracture field, displacement field and velocity field

4.2.1. The evolution law of displacement field, fracture field and velocity field in anchorage body

In this section, the evolution law of microcracks under different vibration load conditions in the process of cyclic load disturbance is analyzed, and the evolution characteristics of displacement field and velocity field are revealed, and then the damage evolution law of anchorage body under different vibration load conditions is studied. The failure process diagram, displacement field and contact force field evolution characteristics corresponding to $T/4$, $T/2$, $3T/4$ and T points in Fig 9 are shown in Figs 10,11 and 12.

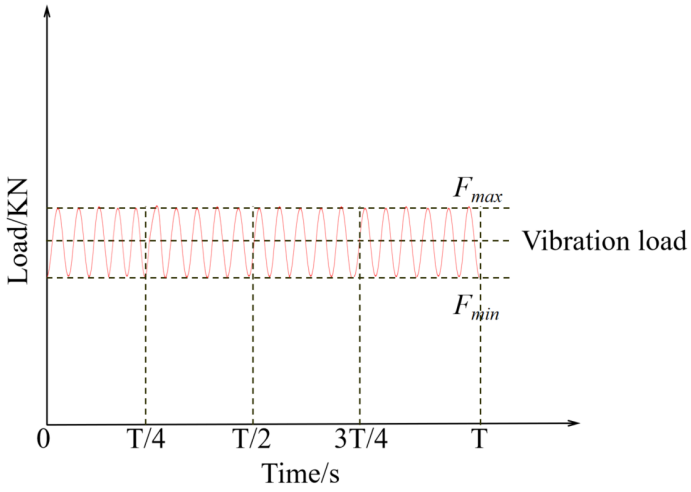

Figure 9. Numerical simulation process of cyclic loading

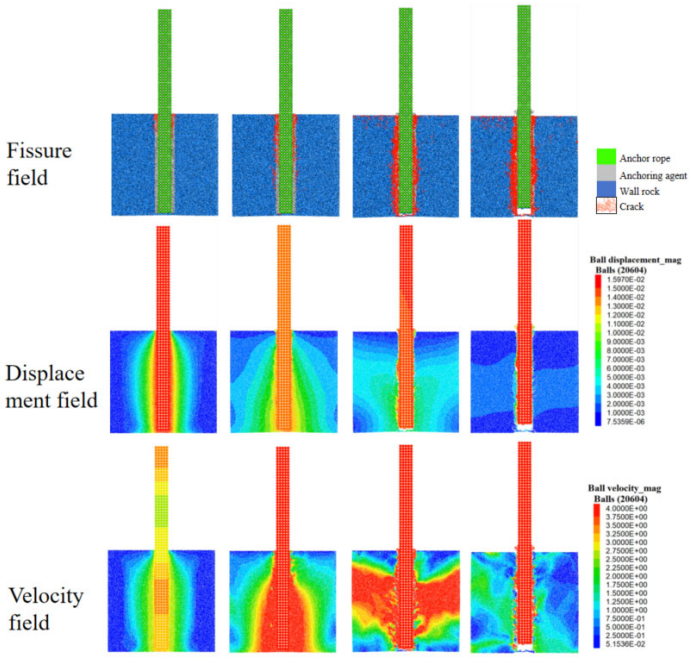

(a) T/4 (b) T/2 (c) 3T/4 (d) T

Figure 10. The evolution characteristics of crack field, displacement field and velocity field of anchorage body under the condition of 40%F vibration load

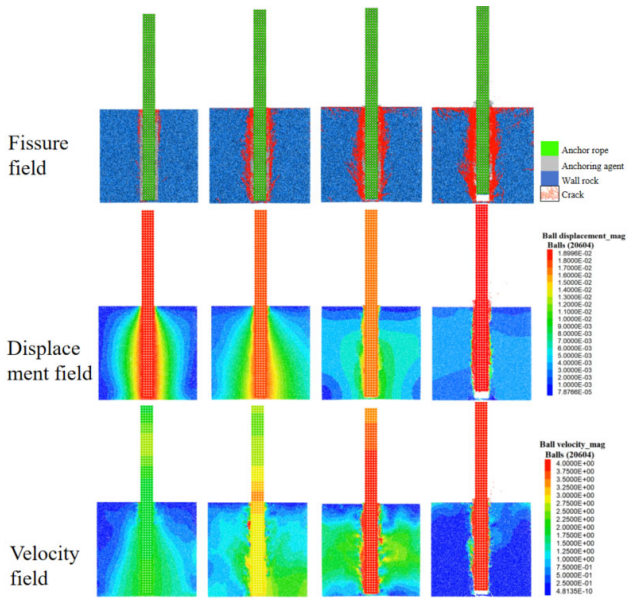

(a) T/4 (b) T/2 (c) 3T/4 (d) T

Figure 11. The evolution characteristics of crack field, displacement field and velocity field of anchorage body under the condition of 50 % *F* vibration load

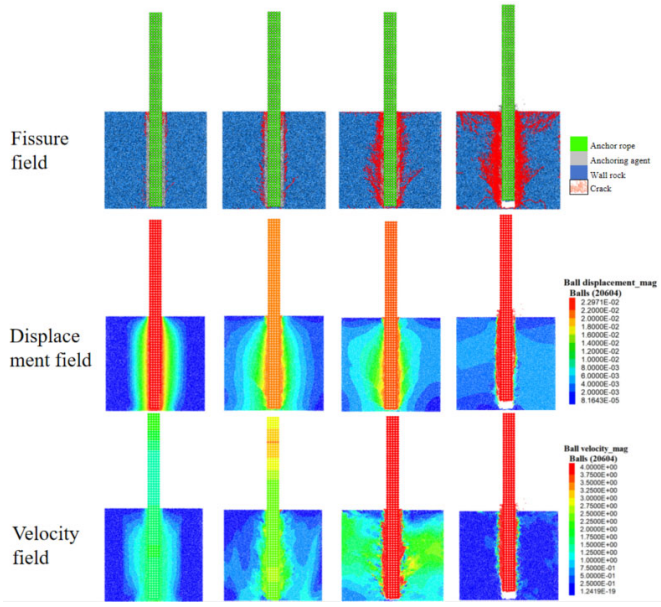

(a) T/4 (b) T/2 (c) 3T/4 (d) T

Figure 12. The evolution characteristics of crack field, displacement field and velocity field of anchorage body under the condition of 60%*F* vibration load

Numerical simulation the cyclic pull-out load along the axial direction is applied to the anchorage body to simulate the whole process of cyclic load disturbance test and destructive pull-out test after disturbance. The evolution law of the internal crack field of the anchorage structure is shown in Fig 10. The internal crack of *T*/4 begins to develop at the top of the anchorage body and propagates downward along the anchorage interface. As the loading time increases to *T*/2, the internal cracks develop along the axial direction of the anchor cable, and the cracks begin to develop from the anchor cable-anchoring agent interface along the radial direction to the anchoring matrix. When the load reaches 3*T*/4, the crack influence area of the anchorage structure continues to increase, and the number of cracks increases. At this time, the anchor cable appears bond slip phenomenon. Finally, at *T*, the crack of the anchoring matrix at the bottom of the borehole is penetrated. At this time, the anchor cable is still bonded and slipped, and cracks appear in the surrounding rock around the anchoring agent and expand outward. Under the condition of 60%*F* vibration load, the upper and middle parts of the anchoring matrix appear through cracks and extend to the surface. The upper crack has penetrated into the surface of the anchoring matrix. The penetration of internal cracks, especially the penetration of upper cracks, is the main reason for the splitting failure of the anchoring matrix. Under the action of cyclic load disturbance, the anchorage ring and surrounding rock are damaged. The cracks are mainly tensile cracks, which are mainly distributed in the anchoring agent layer, the anchor cable-anchoring agent interface and the anchoring agent-anchoring matrix interface.

The evolution process of the displacement field of the anchorage body under the condition of 40%*F*, 50%*F* and

60%F is analyzed, and the results are shown in Fig 11. When loaded to T/4, the vertical displacement field of the anchorage system is consistent with the internal displacement field of the anchorage body under static load drawing, showing the phenomenon of'left and right symmetry, large displacement on the side of the middle anchor cable and the side of the anchoring agent, and the displacement of the surrounding rock on both sides gradually decreases'. When loaded to T/2, the influence area of the internal displacement field of the anchorage body further increases along the radial direction. When loading to 3T/4, the whole anchorage body is in the stage of elastic-plastic deformation, the shallow anchorage interface has been debonding, and the displacement concentration area has moved to the middle and lower part. At this time, the anchorage agent and the surrounding rock have undergone shear deformation and failure, and the displacement field of anchorage body has begun to gradually change into asymmetric distribution. The displacement of anchor cable and anchorage agent begins to be uncoordinated with the displacement of surrounding rock, and the anchorage agent near the anchorage hole has a large displacement. Finally, when loaded to T, the displacement of the anchoring agent-anchor cable combination is significantly larger than that of the surrounding anchoring matrix, indicating that the anchoring system is in the plastic deformation stage at this time, and the anchoring agent-anchoring matrix interface has been debonding. At this time, the anchoring agent has undergone obvious shear deformation damage, and the broken anchoring agent is gradually pulled out as the anchor cable is pulled out. From 40%F vibration load to 60%F vibration load, the overall displacement of anchorage body increases from 15.97mm to 22.97mm.

The evolution process of the velocity field of the anchorage body under the condition of 40%F, 50%F and 60%F is analyzed, and the results are shown in Fig 12. Under the action of axial cyclic load, the particle rate inside the anchorage body is mainly the trend of upward movement of the particles around the anchor cable and the anchoring matrix at the initial stage of loading, and the particle movement rate is large. With the increase of loading time, the influence radius of the velocity field of the anchorage body matrix gradually changes to increase along the radial direction. Finally, due to the debonding of the anchor cable-anchoring agent interface, the anchor cable-anchoring agent is pulled out together, resulting in the internal velocity field changing into the upward movement of the particles in the anchor cable-anchoring agent area, and the particles in the surrounding anchoring matrix do not show the trend of upward movement.

4.2.2. Displacement and shear stress evolution curves of measuring points under different vibration load conditions

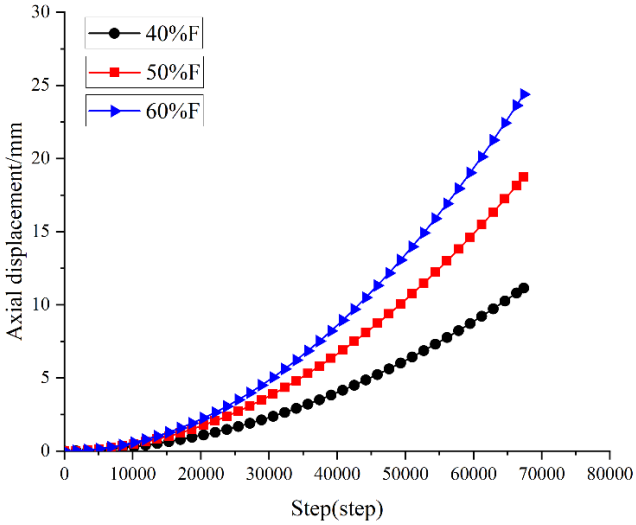

Figure 13. Variation law of axial displacement of anchorage body under different vibration loads

As shown in Fig 13, under the same loading frequency, the vibration load increases from 40%F to 60%F, and the axial displacement of the anchor cable increases from 13.4 mm to 18.7 mm and 24.3 mm. The axial displacement of anchorage body under 60%F vibration load is 1.81 and 1.23 times that of 40%F and 50%F respectively.

In order to observe the stress evolution law of the anchorage system during the pull-out process, the measurement circles were arranged at the depths of 0mm, 30mm, 60mm, 90mm, 120mm and 150m on the interface of the anchor cable-anchorage agent (the first interface) and the interface of the anchor agent-anchorage matrix (the second interface), respectively. The variation of shear stress at the anchorage interface with the analysis step is monitored, as shown in the Fig 14.

It can be seen from the Fig 14 that with the increase of the analysis step, the shear stress of the two anchorage interfaces is transmitted from the shallow to the deep, and the shear stress at a certain depth on the two anchorage interfaces decreases first and then increases. At the same time and at the same depth, the shear stress on the first interface of anchorage is greater than that on the second interface, which confirms the transfer law of shear stress from anchor cable to anchorage agent and then to surrounding rock. There is obvious debonding in the shallow anchorage section of the second interface and the first interface. As the analysis step increases, the debonding section gradually increases. The measurement circle at the top is completely debonded due to the complete debonding failure of the second interface, resulting in a nearly linear distribution of shear stress in the later stage of cyclic loading. The shear stress distribution curve on the first interface shows the same law as that on the second interface, and the debonding time is earlier than that on the second interface.

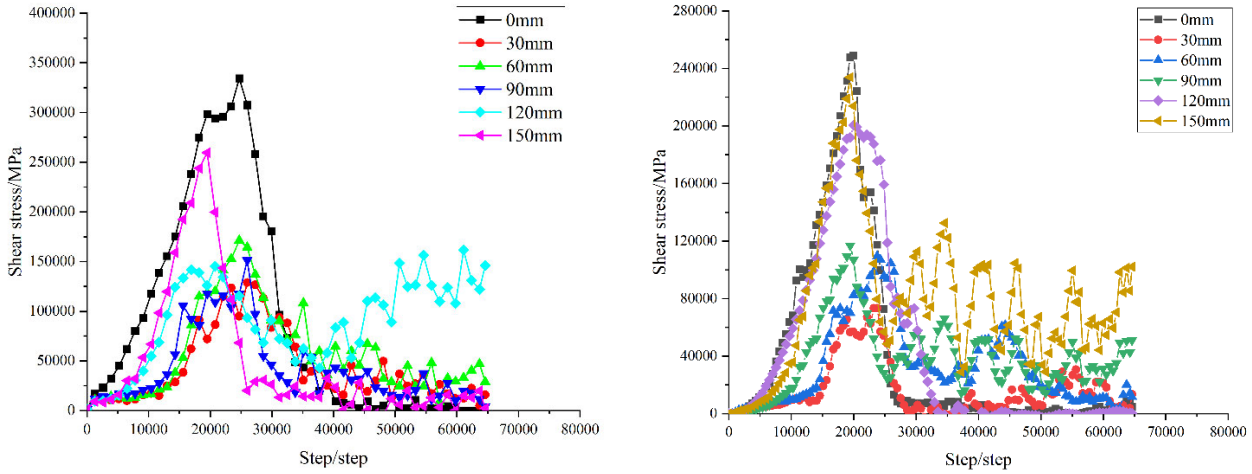

(a) Anchor cable-anchoring agent interface (b) Anchorage agent-anchoring matrix interface

Figure 14. Distribution of interfacial shear stress

4.3. Analysis of fabric characteristics under different vibration load conditions

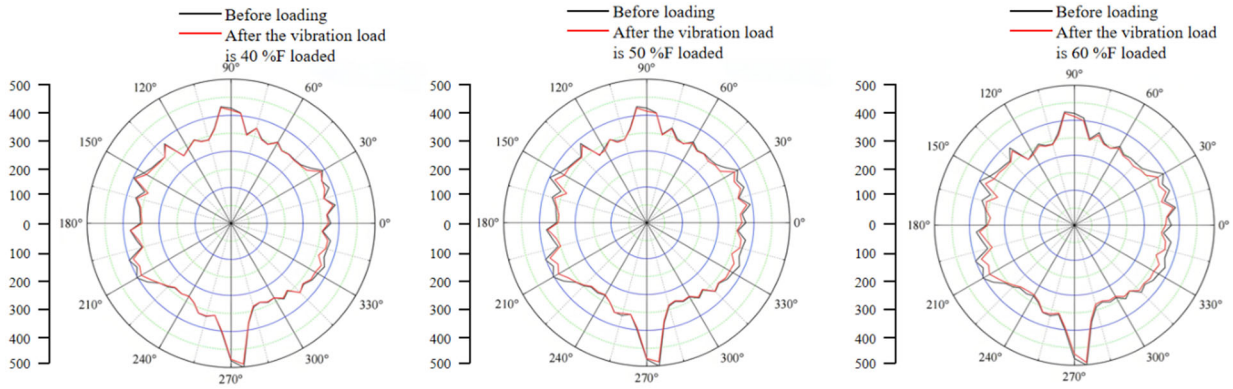

(a) 40%F vibration load (b) 50%F vibration load (c) 60%F vibration load

Figure 15. Analysis of fabric characteristics under different vibration load conditions

The fabric is used to measure the number of particle contacts in the circle that form different angles with the x-axis. Fig 15 shows the change of the fabric of the anchorage under the condition of 40%*F*, 50%*F* and 60%*F* vibration load. Due to the two-way randomness of the particle contact direction, the composition diagram shows an approximate 'centrosymmetric' distribution. In the direction of 180° difference, the contact number shows the same law.

From the analysis of Fig 15, it can be seen that when the vibration load is 40%*F*, the number of particle contact in the 35°(215°) and 152°(332°) directions is significantly reduced, indicating that there are more obvious cracks in these directions; when the vibration load increases to 50%*F*, the number of contacts in the 0°(210°) and 155°(335°) directions further decreases, and there is also a slight decrease in the 3° (183°) direction, indicating that the anchorage interface has undergone significant shear failure at this time, and the degree of damage has increased compared with the 40%*F* load. When the vibration load is 60%*F*, the number of particle contacts in the directions of 0° (180°), 35°(215°) and 145° (325°) decreases to the minimum, which indicates that under the action of 60%*F* load, the anchorage interface has shown signs of crack penetration, and the degree of damage has reached the maximum. During the whole cyclic loading process, the change trend of the internal fabric of the anchorage body is consistent with the evolution law of the fracture field, displacement field and velocity field. Under different vibration load conditions, the damage degree of the anchorage body shows a gradual increase trend, specifically : 60%*F* > 50%*F* > 40%*F*.

4.4. The failure modes of anchorage body under different vibration load conditions

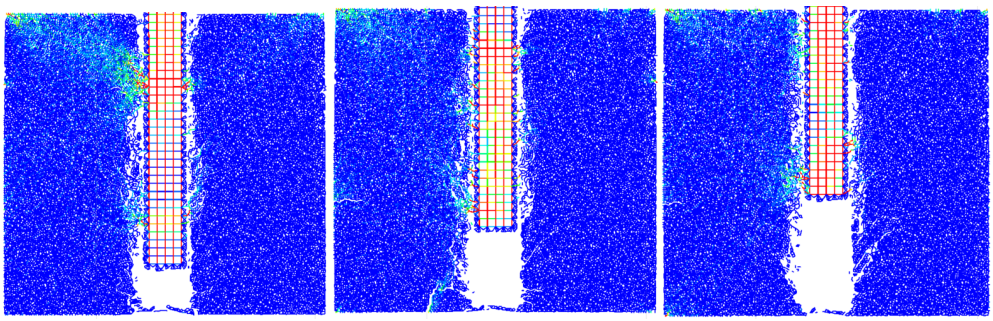

(a) 40%F vibration load (b) 50%F vibration load (c) 60%F vibration load

Figure 16. Contact characteristics of anchorage body force chain under different vibration load conditions

By analyzing the change of the contact force chain between the particles of the anchorage system under cyclic loading, the failure modes of the anchorage body under different vibration load conditions are analyzed. When the contact bond between the particles is destroyed and the contact force chain breaks, it indicates that the bond strength in this area is low. From Fig 16, it can be seen that the contact force chain of the anchor cable-anchorage agent interface and the anchor agent-anchorage matrix interface has been destroyed. Under cyclic loading, both interfaces have debonding phenomenon. As the vibration load increases from 40%F to 60%F, the fracture range of the contact force chain of the anchoring agent and its surrounding anchoring matrix gradually expands. The increase of the load in the vibration leads to the penetration failure of the contact force chain due to the penetration of the macroscopic cracks at the bottom of the anchorage body. Under the condition of high vibration load, the fracture range of the contact force chain of the anchorage matrix is the largest.

5. Damage Law of Anchorage Body Under Orthogonal Parameter Coupling

Table 2. The number of anchored fissures under different coupling parameters

Vibration load	loading frequency				
	1	**5**	**10**	**20**	**30**
30%F	6536	6379	6035	5908	5872
40%F	7520	6850	6320	6236	6108
50%F	8535	7834	7423	7188	6847
60%F	9580	8754	7986	7825	7585
70%F	10356	9356	8934	8245	8183

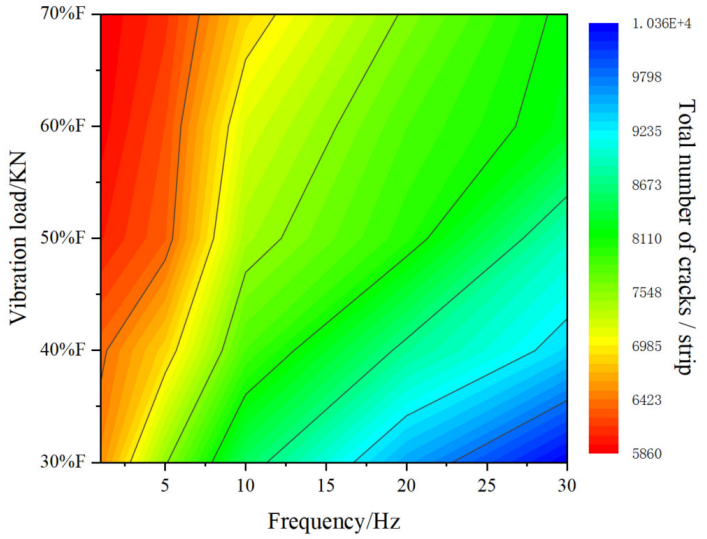

Figure 17. Fracture contour under coupling disturbance of orthogonal parameters

In order to deeply analyze the damage law of anchorage body during cyclic loading with different orthogonal parameters, on the basis of the above simulation results, the influence of multiple cyclic loading condition parameters on the damage degree of anchorage body is further analyzed. The cyclic loading combination conditions of numerical simulation are as follows: the vibration load is 30%F, 40%F, 50%F, 60%F and 70%F respectively, and the loading frequency is 1Hz, 5Hz, 10Hz, 20Hz and 30Hz respectively. Under the above conditions, the numerical simulation test of anchor cable anchorage body under cyclic load is carried out in the orthogonal combination form.

Combined with the numerical simulation results, the relationship between the number of cracks in the model and the coupling parameters is obtained, as shown in Table 2. According to the data in Table 2, the contour map of the total number of cracks under the coupling dynamic load of orthogonal parameters is drawn, as shown in Fig 17. From the

diagram, it can be seen that the influence of high vibration load and low frequency cyclic load on the total number of internal cracks in anchorage body is greater than that of low vibration load and high frequency cyclic load. When the vibration load is 70%F and the frequency is 1Hz, there is only a wide range of crack propagation in the model, which is mainly located in the anchoring agent ring on both sides of the anchor cable and the anchoring matrix near the anchoring agent. When the vibration load is 30%F and the frequency is 30 Hz, the internal cracks of the anchorage body mainly exist in the anchoring agent ring, and there are fewer cracks in the anchoring matrix around the anchoring agent, and the matrix damage degree is higher. The vibration load and low frequency are obviously weakened. As shown in Fig 18.

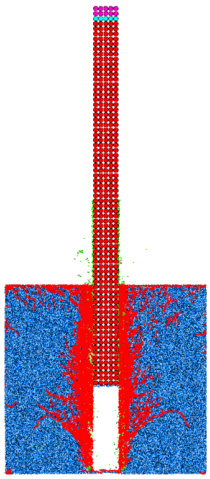

(a) High vibration load, low frequency

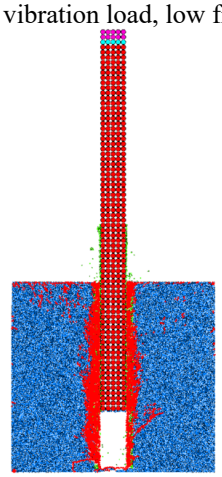

(b) Low vibration load, high frequency

Figure 18. Internal crack propagation of anchorage body under multi-parameter coupled cyclic loading

6. Conclusion

(1) Based on the anchor force model under cyclic loading, it is concluded that there is a close relationship between the debonding displacement of the anchor cable and the dynamic load parameters. The numerical model of anchorage body of anchor cable is established, and the debonding failure process of anchorage body under static load is analyzed. The evolution law of fracture field, displacement field and velocity field in anchorage body under cyclic loading under different vibration load conditions is clarified. The evolution of fracture field in anchorage body is presented as four stages: crack initiation, crack propagation, stable increase and crack penetration.

(2) The crack field, displacement field, velocity field and force chain evolution law of the anchorage system under different vibration load conditions are revealed by applying the axial cyclic load to the anchorage body through numerical simulation. The results show that the crack development begins at the top of the anchorage body and gradually expands along the anchorage interface. The increase of the vibration load accelerates the crack penetration and the failure process of the anchorage system. The displacement field of the anchorage body gradually changes from symmetrical to asymmetrical distribution, and the shallow anchorage interface is debonded. The overall displacement increases significantly with the increase of the vibration load. The shear stress distribution is transmitted from shallow to deep, and the shear stress of the first interface is greater than that of the second interface. The analysis of the contact force chain shows that the increase of the vibration load leads to the expansion of the fracture range of the force chain of the anchoring agent and the matrix, and the failure form is the penetrating splitting failure. The degree of damage gradually increases with the increase of the vibration load.

(3) The damage degree of anchorage body under high vibration load and low frequency cyclic load is higher than that under low vibration load and high frequency load. When the load is 70%F and the frequency is 1Hz, the number of cracks in the anchorage body is the largest, and the anchorage agent and its surrounding matrix are seriously damaged. When the vibration load is 30%F and the frequency is 30Hz, the cracks are mainly concentrated in the anchoring agent ring, and the damage degree of the matrix is small. The difference law of crack propagation in anchorage system under cyclic loading with different orthogonal parameters is revealed.

Acknowledgment

Thank you for the support of Henan University Science and Technology Innovation Talent Support Program Fund (23HASTIT011) for this work.

References

[1] Kang Hongpu, Wu Yongzheng, He Jie, et al. Research and practice of bolt support in deep rock burst roadway [J]. Coal Journal. 2015 : 2225-2233.

[2] Ning Jianguo, Li Zhuang, Wang Jun, et al. Experimental study on mechanical response of anchored solid under dynamic tensile stress wave [J]. Journal of Mining and Safety Engineering, 2022,39 (04) : 731-740.

[3] Chang Jucai, Qi Chao, Yin Zhiqiang, et al. Characteristics of stress wave propagation and damage of fully anchored anchor under dynamic load [J]. Journal of China Coal Society. 2023: 1996-2007.

[4] Chang Jucai, Qi Chao, Yin Zhiqiang, et al. Study on mechanical response characteristics of end-anchored solid under dynamic load [J].Geotechnical mechanics. 2022 : 3294-3304.

[5] ZHANG Nong, WANG Peng, KAN Jiaguang, et al. Experimental study on progressive failure of anchored structures under high-frequency low-energy impact disturbance [J]. Journal of China Coal Society, 2024, 49(01) : 309-319.

[6] Wu Yongzheng, Fu Yukai, Hao Dengyun. Study on dynamic response law of anchored rock mass under lateral impact load [J].Journal of Rock Mechanics and Engineering, 2020,39 (10) : 2014-2024.

[7] Wu Qiuhong, Zhao Fujun, Wang Shiming, etc. Mechanical response characteristics of full-length bonded anchor under dynamic disturbance [J]. Geotechnical mechanics, 2019,40 (03) : 942-950 + 1004.

[8] Chen Miao, Xiao Can, Wang Xiaoshan, et al. Study on mechanical properties and failure mechanism of hole-containing anchorage under dynamic load [J].Journal of Rock Mechanics and Engineering, 1-17 [2024-12-17].

[9] Li Qinghai, Zhang Haoran, Zhou Jian, et al. Study on the mechanism of pre-stressed anchoring and anti-scouring in deep roadway [J].Journal of Mining and Strata Control Engineering, 1-12 [2024-12-17].

[10] Wang Wenjie, Liu Chao, Huang Yongxiang and so on. Analysis of stress and failure characteristics of full-length mortar anchored FRP bolt under dynamic and static loads [J].Geotechnical mechanics : 1-12 [2023-11-01].

[11] Wang Aiwen, Pan Yishan, Zhao Baoyou. Numerical analysis of impact failure mechanism of bolt-surrounding rock structure under impact load [J]. Seismological Engineering, 2017,39 (03) : 417-424.

[12] Zhan Yubao, You Chun 'an, Lu Xingli, etc. Numerical simulation analysis of stress distribution law of anchored solid [C]. 2007 Symposium on hot issues of rock and geotechnical mechanics in ground and underground engineering. 2007.

[13] Xue Yadong, Zhang Shiping, Kang Tianhe. Numerical analysis of dynamic response of bolt in mining roadway [J]. Journal of Rock Mechanics and Engineering, 2003 (11) : 1903-1906.

[14] Zhu Wancheng, Zuo Yujun, Shang Shiming, et al. Numerical simulation of instability and fracture of deep roadway triggered by dynamic disturbance [J]. Journal of Rock Mechanics and Engineering, 2007, 26 (5) : 7.